SANDIA REPORT
SAND2011-7089
Unlimited Release
Printed September 2011

Final Report on LDRD Project: Narrow-Linewidth VCSELs for Atomic Microsystems

Darwin K. Serkland, Weng W. Chow, Kent M. Geib, and Gregory M. Peake

Prepared by
Sandia National Laboratories
Albuquerque, New Mexico 87185 and Livermore, California 94550

Sandia National Laboratories is a multi-program laboratory managed and operated by Sandia Corporation, a wholly owned subsidiary of Lockheed Martin Corporation, for the U.S. Department of Energy's National Nuclear Security Administration under contract DE-AC04-94AL85000.

Approved for public release; further dissemination unlimited.

Sandia National Laboratories

Issued by Sandia National Laboratories, operated for the United States Department of Energy by Sandia Corporation.

NOTICE: This report was prepared as an account of work sponsored by an agency of the United States Government. Neither the United States Government, nor any agency thereof, nor any of their employees, nor any of their contractors, subcontractors, or their employees, make any warranty, express or implied, or assume any legal liability or responsibility for the accuracy, completeness, or usefulness of any information, apparatus, product, or process disclosed, or represent that its use would not infringe privately owned rights. Reference herein to any specific commercial product, process, or service by trade name, trademark, manufacturer, or otherwise, does not necessarily constitute or imply its endorsement, recommendation, or favoring by the United States Government, any agency thereof, or any of their contractors or subcontractors. The views and opinions expressed herein do not necessarily state or reflect those of the United States Government, any agency thereof, or any of their contractors.

Printed in the United States of America. This report has been reproduced directly from the best available copy.

Available to DOE and DOE contractors from
U.S. Department of Energy
Office of Scientific and Technical Information
P.O. Box 62
Oak Ridge, TN 37831

Telephone: (865) 576-8401
Facsimile: (865) 576-5728
E-Mail: reports@adonis.osti.gov
Online ordering: http://www.osti.gov/bridge

Available to the public from
U.S. Department of Commerce
National Technical Information Service
5285 Port Royal Rd.
Springfield, VA 22161

Telephone: (800) 553-6847
Facsimile: (703) 605-6900
E-Mail: orders@ntis.fedworld.gov
Online order: http://www.ntis.gov/help/ordermethods.asp?loc=7-4-0#online

SAND2011-7089
Unlimited Release
Printed September 2011

Final Report on LDRD Project: Narrow-Linewidth VCSELs for Atomic Microsystems

Darwin K. Serkland, Weng W. Chow[2], Kent M. Geib, and Gregory M. Peake

RF/Optoelectronics Technologies Department
[2]Semiconductor Material and Device Sciences Department
Sandia National Laboratories
P.O. Box 5800
Albuquerque, New Mexico 87185

Abstract

Vertical-cavity surface-emitting lasers (VCSELs) are well suited for emerging photonic microsystems due to their low power consumption, ease of integration with other optical components, and single frequency operation. However, the typical VCSEL linewidth of 100 MHz is approximately ten times wider than the natural linewidth of atoms used in atomic beam clocks and trapped atom research, which degrades or completely destroys performance in those systems.

This report documents our efforts to reduce VCSEL linewidths below 10 MHz to meet the needs of advanced sub-Doppler atomic microsystems, such as cold-atom traps. We have investigated two complementary approaches to reduce VCSEL linewidth: (A) increasing the laser-cavity quality factor, and (B) decreasing the linewidth enhancement factor (alpha) of the optical gain medium. We have developed two new VCSEL devices that achieved increased cavity quality factors: (1) all-semiconductor extended-cavity VCSELs, and (2) micro-external-cavity surface-emitting lasers (MECSELs). These new VCSEL devices have demonstrated linewidths below 10 MHz, and linewidths below 1 MHz seem feasible with further optimization.

ACKNOWLEDGMENTS

The authors gratefully acknowledge the expert technical assistance that was provided by Victoria M. Sanchez, Vincent M. Buscema,[*] Thomas M. Bauer,[†] Gordon A. Keeler, J. Bridget Clevenger, Patrick S. Finnegan,[†] Kirt C. Hickman, and Jeffrey Stevens. The authors also thank our managers Charles T. Sullivan and Daniel L. Barton for programmatic support and guidance. Sandia National Laboratories is a multi-program laboratory managed and operated by Sandia Corporation, a wholly owned subsidiary of Lockheed Martin Corporation, for the U.S. Department of Energy's National Nuclear Security Administration under contract DE-AC04-94AL85000.

[*] Sandia Staffing Alliance, LLC
[†] LMATA Government Services, LLC

CONTENTS

1 LDRD Project Introduction 7
  1.1 LDRD Project Overview 7
  1.2 Technical Problem and Approach 7
  1.3 Atomic Spectroscopy using VCSELs 9

2 Extended-Cavity VCSELs 13
  2.1 Introduction 13
  2.2 Standard VCSEL design and linewidth measurement 13
  2.3 All-semiconductor extended-cavity VCSELs 14
  2.4 Summary 16

3 Micro-External-Cavity Surface-Emitting Laser 17
  3.1 Introduction 17
  3.2 MECSEL Design 17
  3.3 MECSEL Fabrication 18
  3.4 MECSEL Device Performance 21
  3.5 Summary 23

4 Linewidth Enhancement Factor Optimization 25
  4.1 Introduction 25
  4.2 Experimental Measurement of Alpha 25
  4.3 Quantum Well Model of the Linewidth Enhancement Factor 26
  4.4 Summary 29

5 Conclusions 30

6 References 31

7 Distribution 33

FIGURES

Figure 1.1. (a) Plot of cold-cavity linewidth versus optical cavity length (n_gL). (b) Bandgap energy and optical field versus distance from the GaAs substrate. 8

Figure 1.2. Cesium valence electron energy levels, not drawn to scale. (a) Schematic diagram showing D1 (894.3 nm) and D2 (852.1 nm) transitions, and the hyperfine splitting of each level. (b) The hyperfine splittings shown relative to a common scale. 10

Figure 1.3. Cesium absorption spectra at (a) 894.3 nm and (b) 852.1 nm. The VCSEL bias current was ramped (red curve) versus time, causing the wavelength to increase from left to right. 10

Figure 1.4. (a) Zoom of L-I resonance dip at 852.1 nm, with oscilloscope trace averaging turned off to show the effects of VCSEL frequency noise. (b) Conversion of VCSEL frequency noise to transmitted amplitude noise when tuned to the edge of the absorption line. 11

Figure 2.1. Standard VCSEL design. (a) Epitaxial structure and simulated standing-wave field profile showing the effective cavity length. (b) Simulated reflection spectrum showing the FWHM cold-cavity linewidth. 13

Figure 2.2. (a) Schematic of the heterodyne setup for measuring VCSEL linewidth. (b) Standard VCSEL linewidth data, which is fitted with a 50-MHz-wide Lorentzian. 14

Figure 2.3. Extended-cavity VCSEL design adds spacer layers near the active region. (a) Epitaxial structure and simulated standing-wave field profile. (b) Simulated reflection spectrum showing the FWHM cold-cavity linewidth. 14

Figure 2.4. . (a) Microscope photograph of EC-VCSEL. (b) Polarization-resolved output power versus current for the EC-VCSEL. 15
Figure 2.5. (a) Optical spectrum of EC-VCSEL. (b) Heterodyne linewidth measurement of EC-VCSEL. 15
Figure 3.1. Schematic (a) cross-section and (b) top views of the MECSEL device. 17
Figure 3.2. (a) Optical mode radius, w, versus mirror radius of curvature, for a fixed cavity length of 25 µm. (b) Simulated optical field profile versus distance z along the axis of the laser beam. .. 17
Figure 3.3. (a) Cross-sectional schematic of the fabricated semiconductor MECSEL base structure. (b) Microscope photograph of resonant-cavity LED emission from the active semiconductor MECSEL base, without an external-cavity mirror. 18
Figure 3.4. (a) MECSEL base output power and voltage versus injected current. (b) Resonant-cavity LED emission spectrum at a drive current of 4 mA. 19
Figure 3.5. Photoresist profiles before and after reflow at 200 °C. (a) Profile of 160- and 120-um diameter photoresist cylinders before reflow. (b) Profile of photoresist after reflow of 160-um diameter cylinder. 19
Figure 3.6. (a) Reflection spectrum of the 6-period dielectric DBR deposited onto a silicon witness wafer. (b) SEM image of photoresist dome covered with a 6-period dielectric DBR. 20
Figure 3.7. (a) Partially released dielectric DBR, showing that the photoresist has been etched from 2 holes at the perimeter of the photoresist dome. (b) SEM image of the partially released dielectric DBR. 20
Figure 3.8. (a) Fully released dielectric DBR dome, after all underlying photoresist was removed using an oxygen plasma. (b) Close-up SEM image of the released dielectric DBR. 21
Figure 3.9. (a) Microscope image of a MECSEL operating with an input current of 4 mA. (b) LIV data of the same MECSEL device, showing a threshold current of 2.1 mA and output power of 2.0 mW at 6 mA input current. 21
Figure 3.10. Light power and wall-plug efficiency versus current for the 10-µm-aperture MECSEL device. 22
Figure 3.11. (a) Polarization-resolved power versus current data, showing a threshold current of 2.1 mA and single-polarization operation to at least 6 mA. (b) Emission spectra at 3 and 4 mA drive current, showing greater than 35 dB side-mode suppression ratio. 23
Figure 4.1. (a) Schematic of heterodyne apparatus used to measure VCSEL AM and FM modulation response. (b) Spectrum analyzer measurement of AM and FM modulation of a VCSEL. 26
Figure 4.2. Two quantum well designs that were modeled: (a) 20% Al barriers, (b) 30% Al barriers. 27
Figure 4.3. Model results for Material gain and Alpha versus Photon energy for two different quantum well designs: (a) 20% Al barriers, (b) 30% Al barriers. 27
Figure 4.4. Linewidth enhancement factor at gain peak versus cladding layer thickness for carrier density between 2 to 3 x 10^{12} cm^{-2} for a structure with three 8nm GaAs QWs and 10nm $Al_{0.2}Ga_{0.8}As$ barriers. The outer barrier layers (cladding layers) are $Al_{0.3}Ga_{0.7}As$ with varying thicknesses. 29

1 LDRD PROJECT INTRODUCTION

1.1 LDRD Project Overview

Single-mode 100-MHz-linewidth vertical-cavity surface-emitting lasers (VCSELs) have recently enabled small low-power atomic sensors, including atomic clocks, magnetometers, and gyroscopes, that rely on spectroscopic interrogation of alkali atoms, typically rubidium or cesium, contained in a gas vapor cell.[1-4] A future generation of higher-performance low-power atomic systems is expected to require substantially narrower VCSEL linewidths (in the range of 1 to 10 MHz) in order to be compatible with the natural atomic linewidth (5 MHz for cesium) that is realized with atomic beams, trapped atoms, and trapped ions. Laser output power above 5 mW in a single mode is also needed for many of these higher-performance atomic sensor applications.

Although DFB and DBR lasers can meet the linewidth and single-mode output power requirements, the typical threshold current exceeds 10mA, which is too high for many battery-powered applications. Alternatively, a conventional optically-pumped vertical-external-cavity surface-emitting laser (OP-VECSEL) can also meet the linewidth and output power requirements,[5] but again it consumes more current than most battery-power applications will tolerate.

Under this LDRD project, we have developed two new types of VCSEL devices which achieve narrower linewidths, but retain the low-power consumption attribute that makes VCSELs especially attractive for many photonic micro-system applications. Both new device types achieve narrower linewidths by increasing the quality factor of the laser cavity, mainly by increasing the effective cavity length while minimizing optical losses. The first new VCSEL device is an all-semiconductor extended-cavity (EC) VCSEL in which additional semiconductor spacer layers are inserted into the epitaxial structure near the optical gain region. This approach has the advantage that relatively few changes to the standard VCSEL micro-fabrication process are required, but the quality factor is limited by the fact that the doped spacer layers necessarily add more round-trip optical loss to the laser cavity. The second new device is a micro-external-cavity surface-emitting laser (MECSEL), in which an external dielectric mirror is micro-fabricated onto the wafer above each laser, increasing each laser cavity length by tens of microns. The MECSEL device has the advantage that larger increases in cavity quality factor can be achieved, but at a cost of a more difficult micro-fabrication process.

All semiconductor lasers, including conventional VCSELs and the new devices developed under this LDRD project, exhibit linewidth broadening due to the linewidth enhancement factor (alpha) of the optical gain region.[6] Under this LDRD project we have studied both theoretically and experimentally the linewidth enhancement factor and how it can be minimized by modifying the quantum well design employed in the optical gain region.[7]

1.2 Technical Problem and Approach

A conventional VCSEL has a relatively large linewidth, on the order of 100 MHz, due primarily to its short effective cavity length of approximately 1.5 microns. To understand how we might reduce the VCSEL linewidth, we digress to consider the fundamental physical mechanisms that determine the linewidth of a semiconductor laser.

A few years before the first laser was demonstrated, Schawlow and Townes predicted its linewidth.[8] Fundamentally, laser linewidth is due to frequency fluctuations that occur when a photon is spontaneously emitted into the laser mode, adding one quantum of electric field at a random phase angle to the existing

laser field. The laser linewidth due to spontaneous emission is given by the modified Schawlow-Townes linewidth formula

$$\Delta\nu_{ST} = (h\nu/P_0)(\pi n_{sp}\eta_0)(\Delta\nu_C)^2, \qquad (1.1)$$

where $\Delta\nu_C$ (≈114 GHz) is the linewidth of the cold cavity (without active region gain or loss), $h\nu$ (≈1.5 eV) is the photon energy, P_0 (≈1 mW) is the output power, n_{sp} (≈2) is the population inversion factor, and η_0 (≈0.5) is the optical output coupling efficiency. In 1982, Henry explained the larger measured linewidths of semiconductor lasers by the formula

$$\Delta\nu = \Delta\nu_{ST}(1+\alpha^2), \qquad (1.2)$$

where α (≈3) is the linewidth enhancement factor of the active region material, which accounts for the fact that carrier density fluctuations in the semiconductor cause refractive index fluctuations that perturb the laser frequency.[6] For a conventional VCSEL structure, a typical lasing linewidth is $\Delta\nu$ = 100 MHz, calculated using the typical parameter values shown in parentheses above.

The short VCSEL cavity length L_C (≈1.5 um) yields a relatively large cold-cavity linewidth $\Delta\nu_C$ (≈114 GHz) in comparison to other lasers, explaining the relatively broad 100 MHz linewidth that a typical VCSEL exhibits. In addition, the low output optical power P_0 (≈1 mW) of VCSELs also prevents them from attaining extremely narrow linewidths.

Extending the cavity length decreases the cold-cavity linewidth according to the formula $\Delta\nu_C = Tc/n_g 2L_C$, as plotted in Figure 1.1(a), where T (≈.004) is the round-trip optical power loss (including output coupling transmission), c is the speed of light, n_g (≈3.5) is the group velocity index, and L_C (≈1.5um) is the effective cavity length. In a conventional VCSEL (parenthetical values), the effective cavity length is dominated by the penetration of the optical fields into the distributed Bragg reflector (DBR) mirrors above and below the active region, as shown in Figure 1.1(b). Optically-pumped vertical-external-cavity surface-emitting lasers (VECSELs) permit extremely long cavity lengths (many centimeters) and have achieved linewidths below 1 MHz, but they are similar in alignment complexity and power consumption to traditional external-cavity diode lasers.

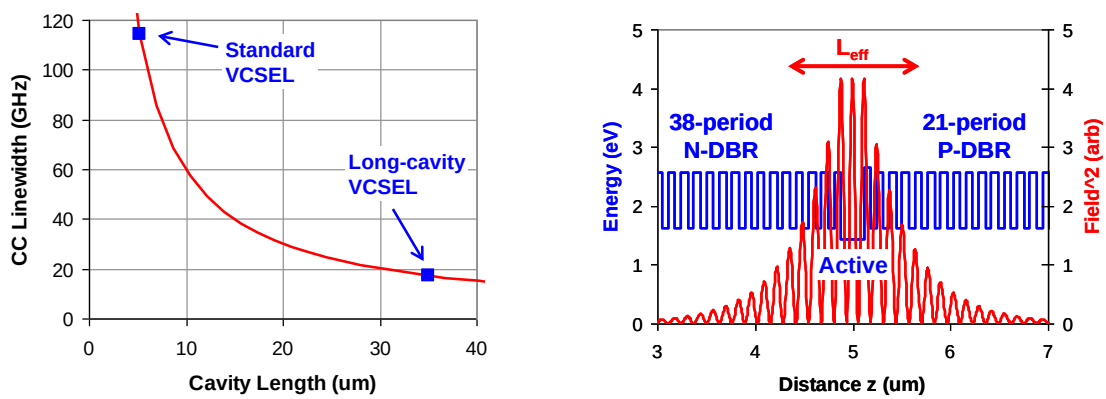

(a) (b)

Figure 1.1. (a) Plot of cold-cavity linewidth versus optical cavity length (n_gL). (b) Bandgap energy and optical field versus distance from the GaAs substrate.

Equations (1.1) and (1.2) suggest a few clear strategies to reduce VCSEL linewidth: increase single-mode output power, decrease cold-cavity linewidth (either by increasing cavity length or decreasing round-trip optical losses), and reduce the linewidth enhancement factor α. Under this LDRD project, we have pursued all of these strategies to some extent. However, the only approach that has the potential to

decrease linewidth by more than an order of magnitude is to increase the cavity length. Therefore, most of our effort was focused on increasing the cavity length to decrease the cold-cavity linewidth, which is equivalent to increasing the cavity quality factor $Q = \nu / \Delta\nu_C$, where ν is the optical frequency of the laser.

1.3 Atomic Spectroscopy using VCSELs

Most recent and emerging atomic microsystems of interest utilize an alkali metal atom (from column I of the periodic table) that has a single valence electron. In particular, Rubidium (Rb) and Cesium (Cs) are most commonly employed in atomic sensors (including atomic clocks) and have atomic transitions at wavelengths accessible with GaAs-based VCSELs, as shown in Table 1.1.

Table 1.1. Rubidium and Cesium D-line wavelengths and ground state hyperfine splitting frequencies. The wavelengths quoted are measured in air.[9]

Element	Isotope	D1 wavelength	D2 wavelength	Hyperfine Splitting
Rubidium	87Rb	794.8 nm	780.0 nm	6 834 682 611 Hz
Cesium	133Cs	894.3 nm	852.1 nm	9 192 631 770 Hz

The alkali metal atoms all have similar spectroscopic features, such as two fundamental optical transitions labeled D1 and D2, from the $^2S_{1/2}$ ground state to the $^2P_{1/2}$ and $^2P_{3/2}$ excited states, respectively. Moreover, the ground state is split into two energy levels separated by the hyperfine splitting, as shown schematically (for Cesium) in Figure 1.2(a). The ground state hyperfine splitting of Cesium is an exact integer 9 192 631 770 Hz, by virtue of the 1967 definition of the second. The hyperfine splitting of Rubidium shown in Table 1.1 is rounded to the nearest Hz.

As an aid to interpreting atomic absorption spectral data, Figure 1.2 shows a moderately detailed energy level diagram of cesium, including the hyperfine splittings of the three lowest energy levels of the valence electron.[10] Figure 1.2(a) shows exaggerated hyperfine splittings and compressed energy level separations (894.3 and 852.1 nm) in order to depict clearly all the energy levels in a single diagram. In Figure 1.2(b) all hyperfine splittings are drawn relative to a common scale, thereby showing the tighter hyperfine spacing of the higher energy levels. Given that the optical frequencies of the D1 and D2 transitions are 335.116 and 351.726 THz, respectively, the energy level separations (894.3 and 852.1 nm) shown in Figure 1.2(b) would have to be increased more than 10,000-fold to be plotted on the same scale as the hyperfine splittings.

Figure 1.3 shows the atomic absorption spectra of cesium at (a) 894.3 nm and (b) 852.1 nm, measured using two different VCSELs. Each absorption spectrum was obtained by shining a VCSEL through a 75-mm-long quartz vacuum cell (no buffer gas), containing atomic cesium at a vapor pressure of approximately 1×10^{-6} torr, obtained at 25°C (room temperature). The VCSEL power was attenuated before the cell, and the light transmitted through the cell was focused onto a New Focus model 2001 silicon photodetector operating at a gain setting $G = 1 \times 10^2$ (transimpedance R = 56 kOhm). For the data shown in Figure 1.3(a), the 894.3-nm VCSEL bias current was fixed at 1.635 mA and a relatively small offset current was ramped (red curve) from -0.07 to +0.07 mA, resulting in an offset wavelength ramp from -0.03 to +0.03 nm, or equivalently an offset frequency ramp from +11 to -11 GHz.

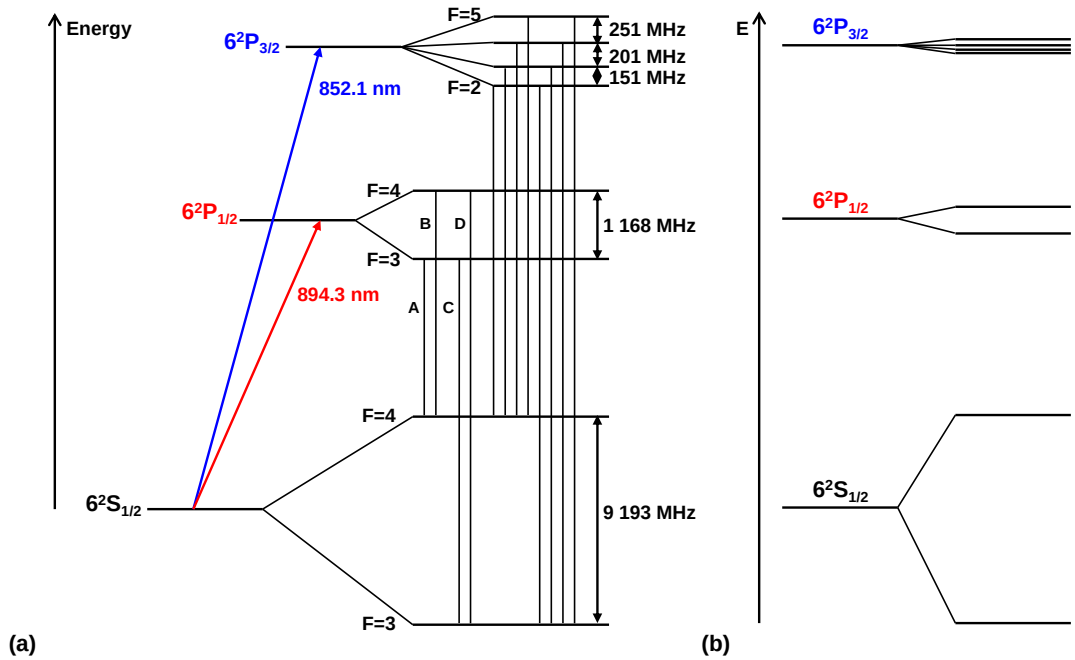

Figure 1.2. Cesium valence electron energy levels, not drawn to scale. (a) Schematic diagram showing D1 (894.3 nm) and D2 (852.1 nm) transitions, and the hyperfine splitting of each level. (b) The hyperfine splittings shown relative to a common scale.

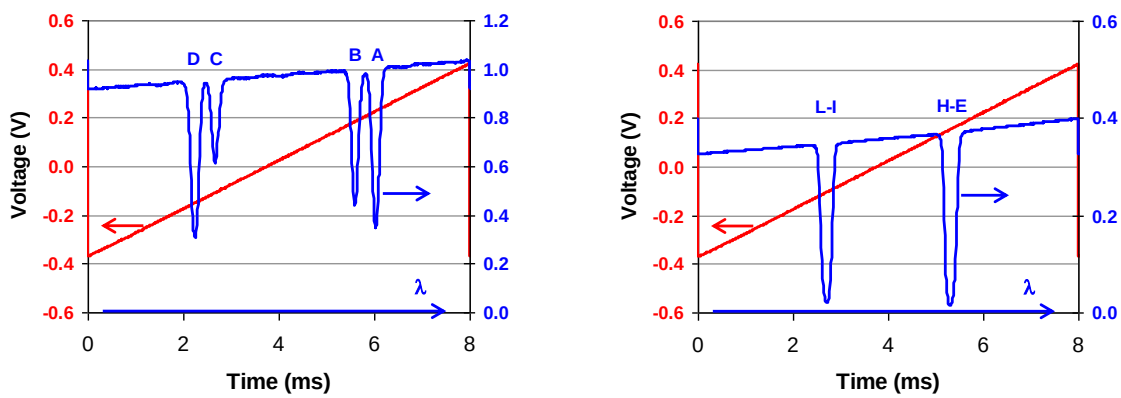

(a) (b)

Figure 1.3. Cesium absorption spectra at (a) 894.3 nm and (b) 852.1 nm. The VCSEL bias current was ramped (red curve) versus time, causing the wavelength to increase from left to right.

The D1 absorption spectrum at 894.3 nm exhibits 4 atomic resonances, labeled A to D, which correspond to the 4 possible transitions between the $6^2S_{1/2}$ and $6^2P_{1/2}$ levels, as shown in Figure 1.2(a). In the 852.1-nm D2 absorption spectrum, shown in Figure 1.3(b), the eight possible transitions appear as only two resolvable resonance dips due to the 600-MHz Doppler broadening of the transitions. The observed left (short-wavelength) 852-nm absorption dip, corresponding to the 4 unresolved transitions from the lower ground state, is labeled L–I, and the right (long-wavelength) 852-nm absorption dip, corresponding to the 4 unresolved transitions from the upper ground state, is labeled H–E. Doppler broadening can be eliminated by reducing the velocity of the atoms relative to the laser beam, either by producing a beam of atoms with velocity vectors orthogonal to the laser beam or by trapping atoms, using a magneto-optic trap (MOT), for example. In this event, all 8 D2 transitions at 852.1 nm would be resolved, and the measured linewidth of each transition would be limited by the VCSEL linewidth (typically about 100 MHz).

Most atomic sensors employ alkali metal vapor cells, such as the cesium cell described above. Often a buffer gas, such as nitrogen, is added to reduce the effects of atoms colliding with the cell walls. In vapor cells, the atomic resonance lines are Doppler broadened. The addition of a buffer gas further broadens the width of the resonance due to pressure broadening. However, VCSEL frequency fluctuations generally limit the performance (noise floor) of the sensor, even though the VCSEL linewidth (100 MHz) is typically less than the atomic linewidth (>600 MHz). The reason is that the atomic absorption profile versus frequency converts FM noise on the VCSEL to AM noise on the transmitted laser beam. In order to illustrate this effect, we zoomed in on the left (L–I) resonance dip in Figure 1.3(b), by changing the VCSEL bias current from 1.215 to 1.190 mA and reducing the offset current ramp amplitude 8-fold, as shown in Figure 1.4(a). For the data shown in Figure 1.4, we turned off trace averaging on the oscilloscope to see the full effect of VCSEL frequency noise.

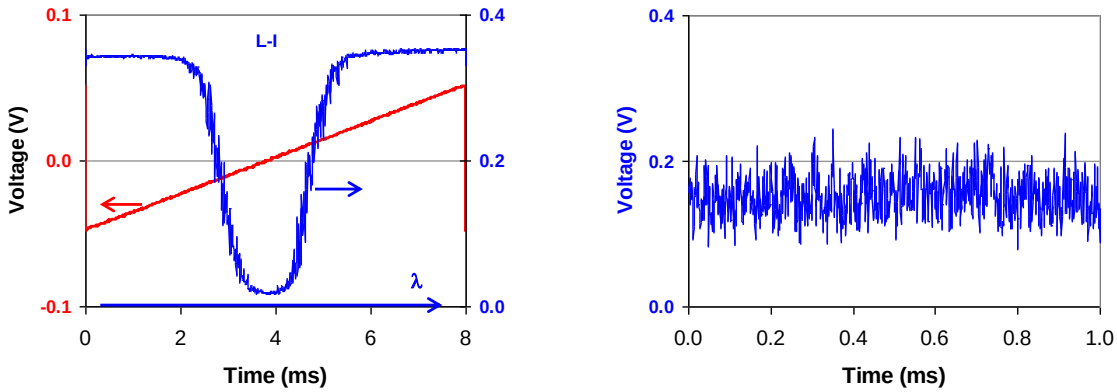

(a) (b)

Figure 1.4. (a) Zoom of L-I resonance dip at 852.1 nm, with oscilloscope trace averaging turned off to show the effects of VCSEL frequency noise. (b) Conversion of VCSEL frequency noise to transmitted amplitude noise when tuned to the edge of the absorption line.

On the edges of the resonance line shown in Figure 1.4(a), frequency fluctuations of the VCSEL are converted to amplitude fluctuations of the transmitted laser beam. In a sensor application, the laser frequency is typically locked to the atomic resonance frequency. In Figure 1.4(b), the VCSEL offset current ramp was turned off and the fixed bias current was reduced to 1.187 mA in order to tune the VCSEL to the short-wavelength side of the resonance dip shown in Figure 1.4(a). At the edge of the absorption line, FM noise on the VCSEL is linearly converted to AM noise on the transmitted beam. Fortunately, many atomic sensors lock the VCSEL to the exact line center, in which case the FM to AM conversion is greatly reduced, because the linear conversion coefficient is zero, and a weaker quadratic term comes into play.[1] But some amount of FM to AM noise conversion is always present, and this noise source typically sets the noise floor for VCSEL-based atomic sensors. Thus, to the extent that VCSEL frequency noise (linewidth) can be reduced, the noise floor of atomic sensors will decrease, and the signal-to-noise ratio will increase.

If the VCSEL linewidth could be reduced below the natural atomic linewidth (5 MHz for Cesium), it would allow the use of VCSELs in higher performance atomic systems, such as the NIST F1 atomic fountain clock, which is considered among the most accurate primary frequency standards in the world.[11] The NIST F1 clock employs laser-cooled Cesium atoms, which due to their low velocity, exhibit natural atomic linewidths of 5 MHz. Most laser cooling and trapping experiments employ external-cavity diode lasers (ECDLs) with linewidths below 1 MHz. External-cavity diode lasers typically consist of an anti-reflection-coated edge-emitting laser chip and an external grating placed a few centimeters away to act as a frequency selective mirror. Such lasers require precise and costly mechanical alignment, occupy a large (>100 cm^3) volume, and consume significant (>100 mW) electrical

power, practically prohibiting their application in battery-powered low-cost atomic systems. Thus, if VCSEL linewidth could be reduced below 5 MHz, it would open up new applications in high-performance Doppler-free atomic systems.

2 EXTENDED-CAVITY VCSELS

2.1 Introduction

As described in Section 1.2, any increase in the effective cavity length will decrease the linewidth, assuming that other parameters (such as the round-trip cavity loss can be held constant). In this section we describe a method to increase the effective length solely by changing the epitaxial semiconductor layer structure of a conventional VCSEL. Specifically, we show how adding cavity spacer layers can increase the effective cavity length without significantly increasing the cavity losses.

2.2 Standard VCSEL design and linewidth measurement

We have previously reported the development of 50-MHz linewidth VCSELs at 852.1 and 894.3 nm for chip-scale atomic clock applications.[12] In order to achieve those results, we reduced the linewidth enhancement factor by detuning the cavity resonance from the optical gain peak wavelength. The structure of this relatively standard VCSEL is shown in Figure 2.1(a), along with the simulated optical field profile near the active region, showing the effective cavity length penetrating into the lower and upper DBR mirrors. This standard VCSEL structure has a cold-cavity linewidth ($\Delta\lambda$ = 0.24 nm), as shown by the simulated reflection spectrum in Figure 2.1(b).

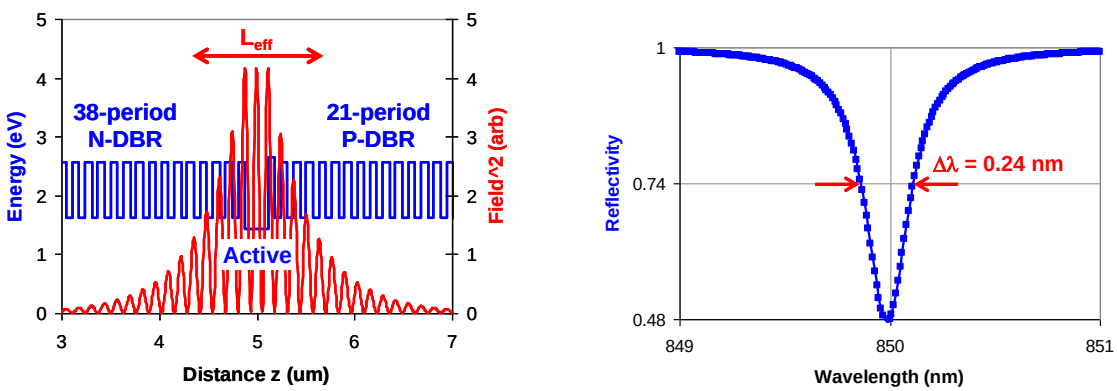

(a) (b)

Figure 2.1. Standard VCSEL design. (a) Epitaxial structure and simulated standing-wave field profile showing the effective cavity length. (b) Simulated reflection spectrum showing the FWHM cold-cavity linewidth.

Figure 2.2(a) shows a schematic diagram of the optical heterodyne measurement setup that we employed to measure the linewidth of the standard 850-nm narrow-linewidth VCSEL design described above. For this measurement, an external-cavity diode laser (EOSI, linewidth < 1 MHz) at 850-nm was tuned to a frequency f_1, approximately 1 GHz below the VCSEL frequency f_2. The two optical beams were combined using a 50% beam splitter and coupled into an 850-nm single-mode fiber and detected with a 12-GHz photoreceiver (New Focus model 1580-B) whose output was fed into an electrical spectrum analyzer. The spectrum analyzer resolution bandwidth was set at 2 MHz. The resulting beat note appeared at approximately 0.85 GHz, as shown in Figure 2.2(b). A Lorentzian with a 50-MHz FWHM linewidth fits the data well. The VCSEL drive current for this measurement was 1.5 mA, which was supplied by a low-noise current source. Also, the VCSEL was temperature stabilized in an oven to minimize thermal frequency drifts during the measurement.

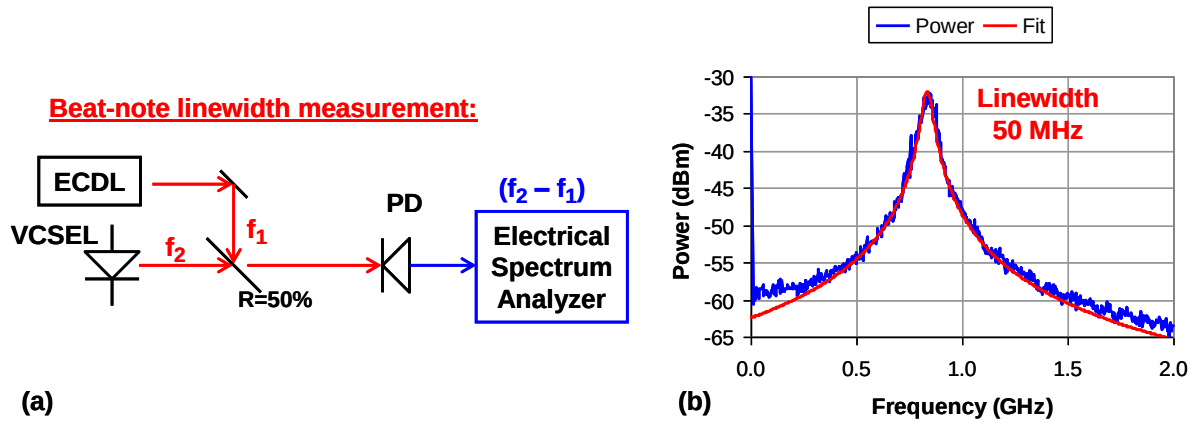

Figure 2.2. (a) Schematic of the heterodyne setup for measuring VCSEL linewidth. (b) Standard VCSEL linewidth data, which is fitted with a 50-MHz-wide Lorentzian.

2.3 All-semiconductor extended-cavity VCSELs

A particularly simple and effective means of achieving a roughly 4-fold reduction in laser linewidth is to fabricate an all-semiconductor extended-cavity (EC) VCSEL, as shown in Figure 2.3(a), where one or more semiconductor spacer layers are added near the optical gain region in order to increase the effective cavity length. This extended-cavity approach is motivated by the formula $\Delta\nu_C = Tc/n_g 2L_C$, which shows that the cold-cavity linewidth scales as the inverse of the effective cavity length. Figure 2.3(a) shows the simulated optical field profile near the active region, exhibiting a significant (nearly 100%) increase in the effective cavity length relative to the standard VCSEL design. The cavity extension must be made such that it does not significantly increase the round-trip optical loss if it is to be effective at reducing the cold-cavity linewidth, according to the formula above. For this reason, we chose to incorporate the cavity length extension layers in the n-type DBR (rather than p-type DBR) to minimize free carrier absorption in the extension layers. This extended-cavity VCSEL structure achieves a 48% reduction in cold-cavity linewidth relative to the standard VCSEL structure described previously, as shown by the simulated reflection spectrum in Figure 2.3(b). Our simulations assume a 30/cm optical absorption coefficient for the cavity extension layer. The reduction in cold-cavity linewidth depends critically on minimizing the losses in the cavity extension layers.

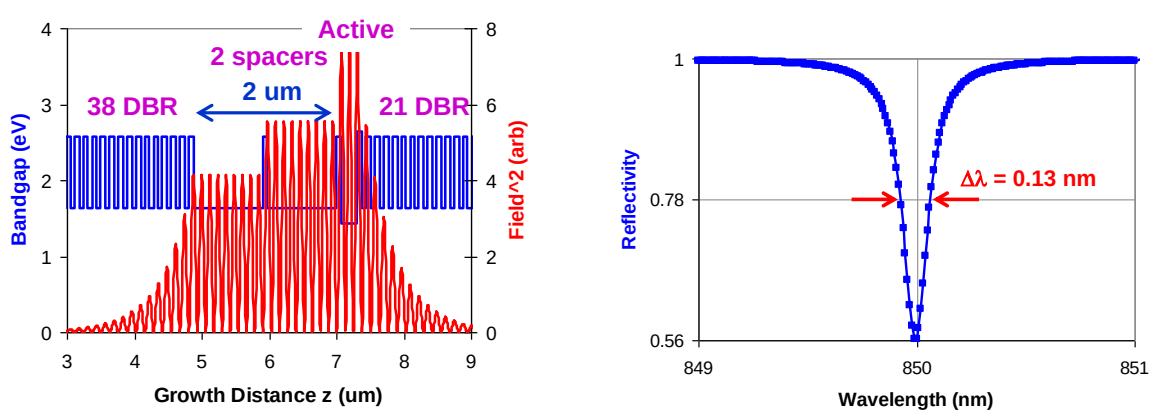

(a) (b)

Figure 2.3. Extended-cavity VCSEL design adds spacer layers near the active region. (a) Epitaxial structure and simulated standing-wave field profile. (b) Simulated reflection spectrum showing the FWHM cold-cavity linewidth.

The fabricated all-semiconductor EC-VCSEL is shown in Figure 2.4(a). Although the epitaxial structure is a few microns thicker, the micro-fabrication process is essentially identical to that of a standard VCSEL. Figure 2.4(b) shows the polarization-resolved output power of the EC-VCSEL versus current. It is notable that the EC-VCSEL achieves a relatively high single-mode output power of 2.5 mW, which also helps to reduce the laser linewidth according to the theory presented in section 1.2.

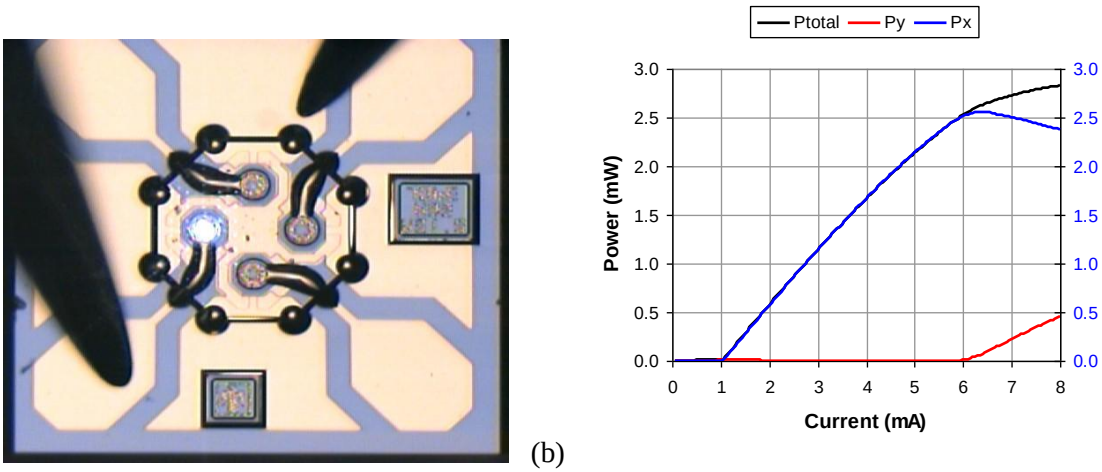

(a) (b)

Figure 2.4. . (a) Microscope photograph of EC-VCSEL. (b) Polarization-resolved output power versus current for the EC-VCSEL.

The output optical spectrum of the EC-VCSEL (operating at 3 mA drive current) is shown in Figure 2.5(a), which shows that the laser maintains single-transverse-mode operation with a side-mode suppression ratio of 34 dB. The EC-VCSEL linewidth was measured by the heterodyne beatnote method described previously. Figure 2.5(b) shows the measured beatnote at 0.4 GHz. A Lorentzian with an 8.5-MHz linewidth fits the data well, as shown in Figure 2.5(b). According to the simulations, the reduction in cold-cavity linewidth by almost 50% should yield a nearly 4-fold decrease in linewidth, from 50 to 13 MHz. The increased single-mode output power explains the additional linewidth reduction to 8.5 MHz.

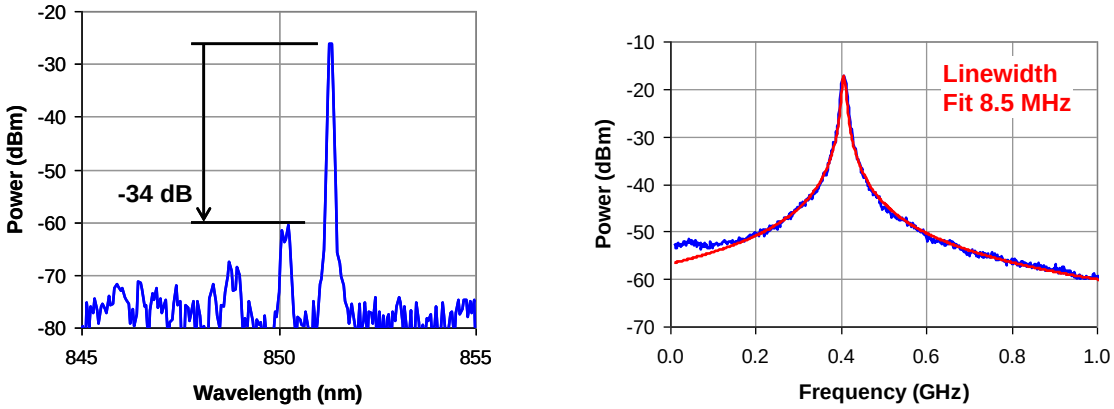

(a) (b)

Figure 2.5. (a) Optical spectrum of EC-VCSEL. (b) Heterodyne linewidth measurement of EC-VCSEL.

2.4 Summary

In summary, we have demonstrated a five-fold reduction in VCSEL linewidth (from 50 to 8.5 MHz) obtained primarily by adding a cavity length extension layer to a standard oxide-confined 850-nm VCSEL structure. This result verifies the expected linewidth scaling versus cavity length, and provides a method of narrowing VCSEL linewidth that can be used in addition to reducing cavity losses and reducing the linewidth enhancement factor of the active region. Simulations show that it is critical to fabricate the cavity extension layers such that they add minimal additional loss to the cavity, otherwise the benefit of increased cavity length can be lost.

3 MICRO-EXTERNAL-CAVITY SURFACE-EMITTING LASER

3.1 Introduction

In this section we will discuss the design and fabrication of the micro-external-cavity surface-emitting laser (MECSEL) device, shown schematically in Figure 3.1. The figure shows an example using an external-cavity length of 25 µm from the semi-conductor surface to the external mirror, which has a radius of curvature of 130 µm.

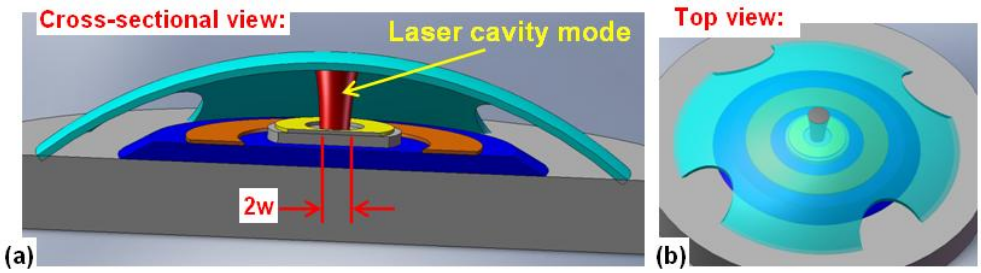

Figure 3.1. Schematic (a) cross-section and (b) top views of the MECSEL device.

3.2 MECSEL Design

The process that we employed to micro-fabricate the external curved mirror (to be discussed later) yields a relatively short external cavity length of approximately 25 µm. For a plano-concave cavity length fixed at 25 µm, Figure 3.2(a) shows the calculated mode radius (at the $1/e^2$ intensity point) at the flat (semiconductor) mirror surface.[13] For example, for an external mirror having a radius of curvature of 130 µm, the calculated optical mode diameter at the semiconductor active layers is 7.6 µm. The MECSEL mode diameter of 7.6 µm is approximately twice that of a typical single-mode oxide-aperture VCSEL, suggesting that such a MECSEL could extract four times the single-mode output power of a VCSEL. The cost of the increase in output power will be an increase in threshold current, which will increase with the area of the semiconductor current aperture.

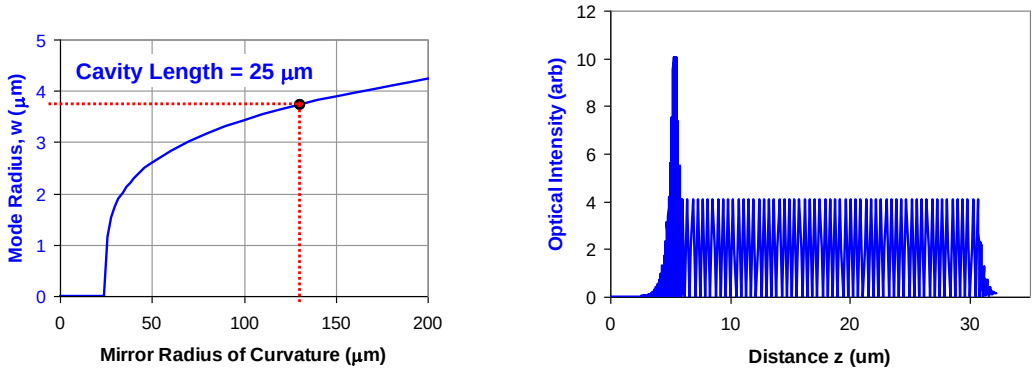

(a) (b)

Figure 3.2. (a) Optical mode radius, w, versus mirror radius of curvature, for a fixed cavity length of 25 µm. (b) Simulated optical field profile versus distance z along the axis of the laser beam.

Additionally, the effective cavity length is increased approximately 10-fold, as shown by the 1-D field profile simulation in Figure 3.2(b). A 10-fold increase in effective cavity length relative to a VCSEL will decrease the cold-cavity linewidth 10-fold and will decrease the lasing linewidth 100-fold.[6,8] Thus, we can expect to reduce the linewidth from 100 MHz for a narrow-linewidth VCSEL to approximately 1 MHz for a narrow-linewidth MECSEL.

3.3 MECSEL Fabrication

A schematic cross-sectional view of the fabricated semiconductor MECSEL base structure is shown in Figure 3.3(a). The active region contains 5 GaAs quantum wells of thickness 8 nm, positioned at a maximum of the standing wave optical field. The bottom distributed Bragg reflector (DBR) consists of 39 pairs of quarter-wave 16% and 92% AlGaAs layers, yielding a reflectivity above 99.9%. A partial top DBR consists of 8 pairs of quarter-wave 16% and 92% AlGaAs layers, resonating the optical gain provided by the quantum wells. The top DBR is doped p-type, the bottom DBR is doped n-type, and ohmic contacts are applied to each DBR to permit injection of carriers into the quantum wells to create optical gain near 850 nm. Hydrogen ions are implanted around the perimeter of the top p-type DBR mesa to increase the electrical resistance except within the current aperture of diameter D. For this study a range of implant current aperture diameters were fabricated, from 6 to 12 µm, with the intent of matching the plano-concave optical-cavity mode diameter of approximately 8 µm. Figure 3.3(b) shows a microscope photograph of the MECSEL base structure, with resonant LED emission coming from within the implant aperture diameter D = 12 µm at a bias current of 3 mA.

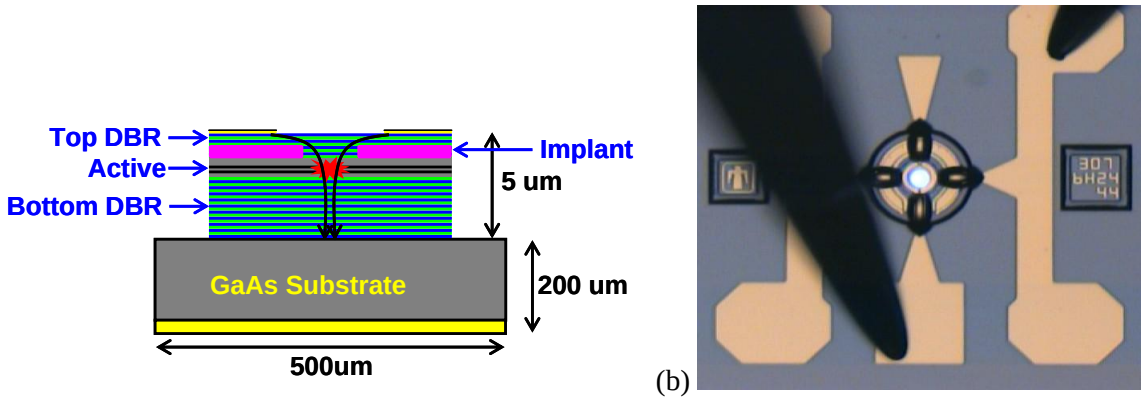

Figure 3.3. (a) Cross-sectional schematic of the fabricated semiconductor MECSEL base structure. (b) Microscope photograph of resonant-cavity LED emission from the active semiconductor MECSEL base, without an external-cavity mirror.

The electrical and optical device characteristics of the active semiconductor MECSEL base structure, with implant aperture diameter of 12 µm, are shown in Figure 3.5. The series resistance of the device is higher than intended due to a problem with the ion implant energy and fluence and because of high lateral spreading resistance in the low-mobility p-type top DBR layers.

The curved external mirror was fabricated by depositing a dielectric DBR stack onto a spherical photoresist dome. The photoresist dome was fabricated by spinning 20-µm-thick photoresist and patterning circles (cylinders) concentric relative to the implant apertures using a standard photolithography process. The concentric alignment accuracy of the photoresist cylinders relative to the implant apertures is determined by the photomask alignment. Using our contact mask aligners, relative alignment accuracy on the order of 1 µm is achieved, but better accuracy could be obtained by using a "stepper" mask aligner. Given that the calculated optical mode diameter is about 8 µm, an alignment

accuracy of 1 µm should be adequate to yield maximal overlap between the fundamental Gaussian optical mode and the implant gain aperture.

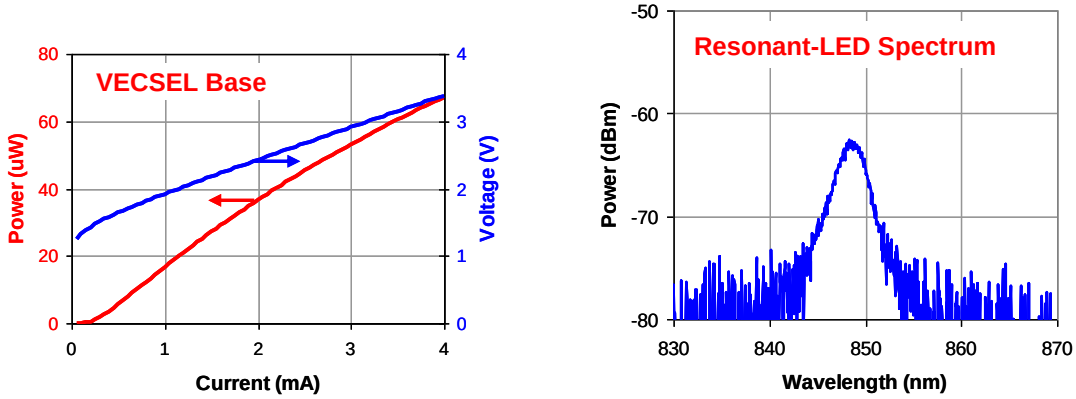

(a) (b)

Figure 3.4. (a) MECSEL base output power and voltage versus injected current. (b) Resonant-cavity LED emission spectrum at a drive current of 4 mA.

The profile of two patterned photoresist cylinders of diameter 160 and 120 µm is shown in Figure 3.5(a). The patterned photoresist height measured 20 µm before being reflowed. We reflowed the photoresist by heating it to 200 °C in 2 minutes, and holding at 200 °C for another 2 minutes before cooling to room temperature. The profile of a reflowed 160-µm-diameter cylinder is shown in Figure 3.5(b). As expected, the reflowed photoresist surface is spherical, as demonstrated by the close agreement with the spherical curve fit shown (in red) in Figure 3.5(b). For this particular photoresist dome, the radius of curvature was measured to be 131 µm, which is the value chosen in our example calculations above. The height of the photoresist dome increased from 20 µm before reflow to 28 µm after reflow. We have modeled the photoresist reflow process and obtained excellent agreement with measurements, assuring us that the process is far more reproducible than necessary for our purposes. We note that the Gaussian optical mode diameter is not particularly sensitive to either the radius of curvature or the dome height for our chosen design point.

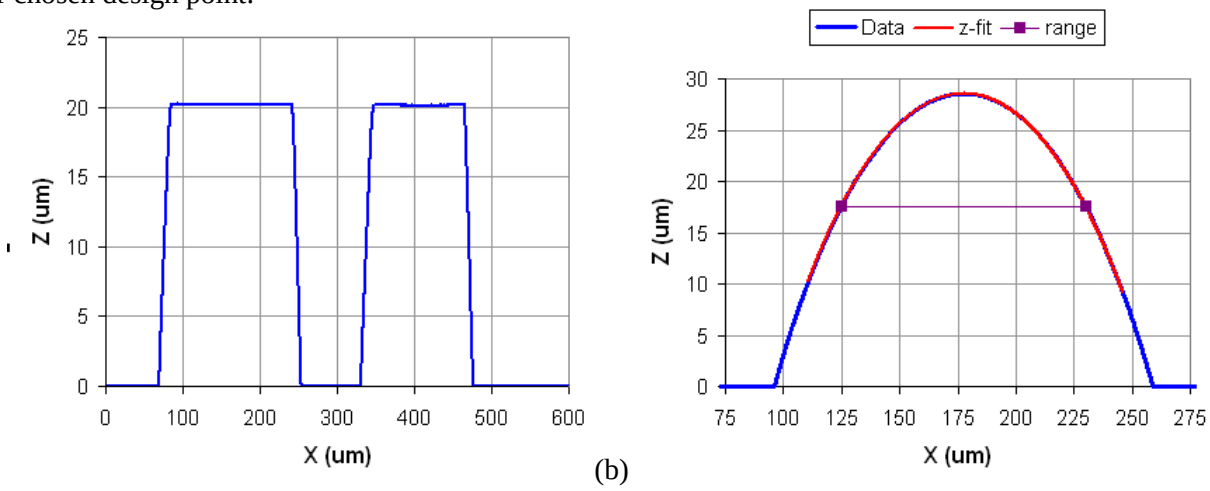

(a) (b)

Figure 3.5. Photoresist profiles before and after reflow at 200 °C. (a) Profile of 160- and 120-um diameter photoresist cylinders before reflow. (b) Profile of photoresist after reflow of 160-um diameter cylinder.

Plasma-enhanced chemical-vapor deposition (PECVD) was employed to deposit a 6-period dielectric DBR onto the reflowed photoresist domes. The dielectric DBR consisted of 6 pairs of quarter-wave layers of silicon dioxide (SiO_2, n=1.46) and silicon nitride (SiN, n=1.96). The measured reflection

spectrum of the dielectric DBR, deposited onto a witness silicon wafer, is shown in Figure 3.6(a). The reflectivity at the center of the stop band was 97% on the silicon wafer, and simulations predict a reflectivity of 90% for the same DBR stack suspended in air (after the photoresist is removed). The center wavelength of the as-deposited dielectric DBR was shorter than the VCSEL design wavelength of 850 nm over most of the sample, which reduced the yield of our fabrication run. In order to remove the photoresist from under the curved dielectric DBR, we patterned photoresist over the DBR dome, opening four holes at the perimeter of each photoresist dome. The dielectric DBR was etched through those four holes, exposing the photoresist at the perimeter of the dome, as shown in Figure 3.6(b).

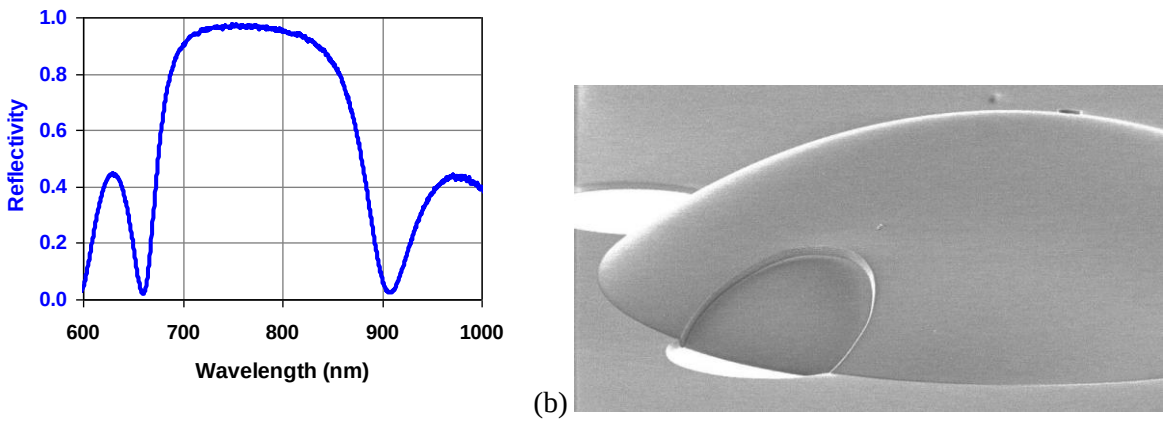

Figure 3.6. (a) Reflection spectrum of the 6-period dielectric DBR deposited onto a silicon witness wafer. (b) SEM image of photoresist dome covered with a 6-period dielectric DBR.

The photoresist dome was removed from under the dielectric DBR by ashing in an oxygen plasma at 120 °C for 2 hours. Figure 3.7(a) shows a microscope image of a dielectric DBR dome that was partially plasma released. The microscope image clearly shows where the photoresist was removed through two holes in the dielectric DBR at the perimeter of the dome. The other two intended holes, visible in the photograph, did not fully penetrate the DBR, and hence the oxygen plasma could not remove the photoresist from those access points. The microscope ring-light illuminator is visible as reflected from the top curved surface (white) and from the flat semiconductor surface (yellow). Figure 3.7(b) shows a scanning electron microscope (SEM) image of another partially released dielectric DBR dome.

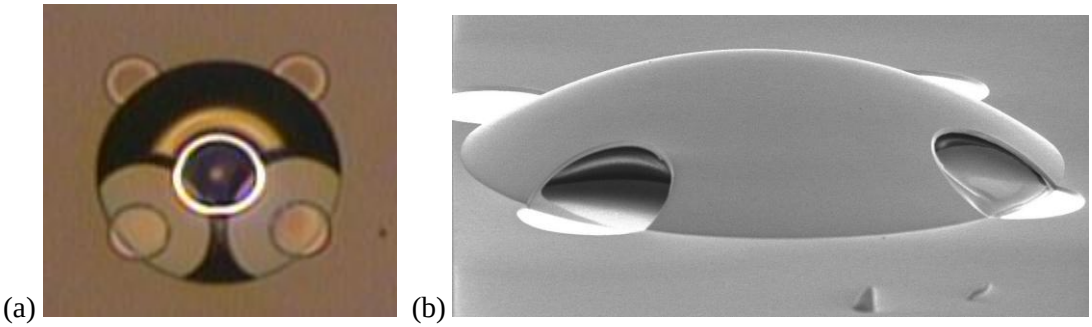

Figure 3.7. (a) Partially released dielectric DBR, showing that the photoresist has been etched from 2 holes at the perimeter of the photoresist dome. (b) SEM image of the partially released dielectric DBR.

A fully released dielectric DBR dome, with all of the underlying photoresist removed, is shown in Figure 3.8(a). A close-up SEM image of the released dielectric DBR dome, at the edge of a release hole, is shown in Figure 3.8(b). The 6 periods of the dielectric DBR are clearly visible in this SEM micrograph.

Although the dielectric DBR thickness was only 1.5 µm, and the dome spanned a base diameter of 160 µm, the released dielectric DBR domes appeared to be mechanically robust with no visible damage except where tweezers contacted the wafer or where the photoresist patterns were defective. We anticipate a fundamental mechanical resonance frequency of the dielectric DBR membrane on the order of 1 MHz, based on comparisons with similar MEMS structures reported in the literature. In the future, we intend to use transparent optical epoxy to under-fill the dielectric DBR domes, in order to improve mechanical robustness of the structure and strongly damp the vibrational resonance of the suspended dielectric membrane.

(a) 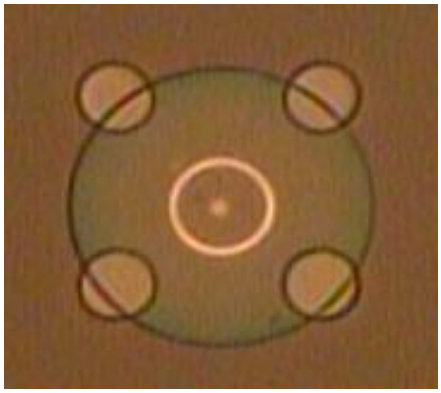 (b) 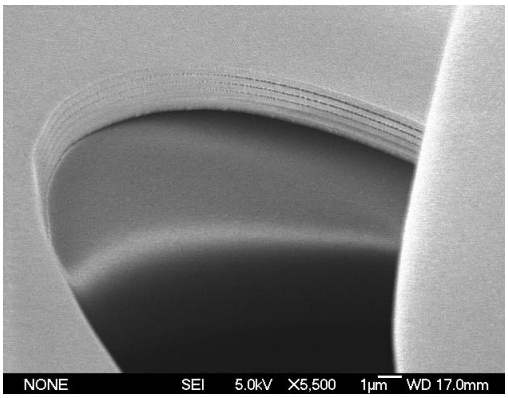

Figure 3.8. (a) Fully released dielectric DBR dome, after all underlying photoresist was removed using an oxygen plasma. (b) Close-up SEM image of the released dielectric DBR.

3.4 MECSEL Device Performance

We fabricated a released dielectric DBR dome over a MECSEL base structure, as described in the previous section, yielding the MECSEL device shown in Figure 3.9(a). The photograph shows the MECSEL lasing with an input drive current of 4 mA. The implant aperture diameter for this particular MECSEL was 10 µm. Light power (L) and voltage data (V) versus current for this same device are shown in Figure 3.9(b). The threshold current was 2.1 mA and the peak output power was 2 mW at a drive current of 6 mA. The series resistance of this device was high (472 Ω), which was due to

(a) 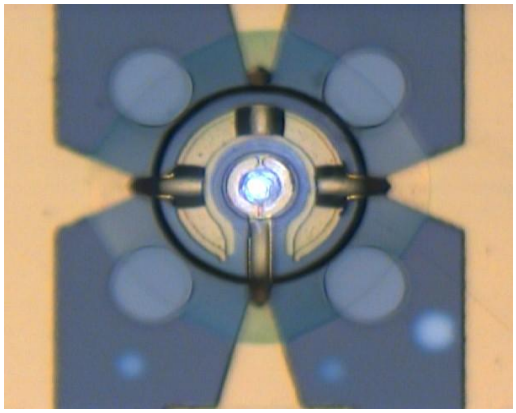 (b) 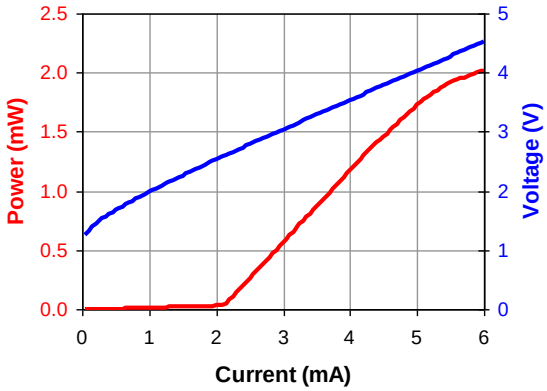

Figure 3.9. (a) Microscope image of a MECSEL operating with an input current of 4 mA. (b) LIV data of the same MECSEL device, showing a threshold current of 2.1 mA and output power of 2.0 mW at 6 mA input current.

the implant problem and spreading resistance in the low-mobility p-type material, as discussed previously. Because the as-deposited dielectric DBR wavelength was shorter than the 850-nm MECSEL base wavelength over most of the wafer surface, the yield from this fabrication run was relatively low. The only lasing devices were found near the rim of the wafer, where the MECSEL base wavelength fell below 850 nm and the dielectric DBR wavelength rose above 800 nm. Nonetheless, it is notable that our very first fabrication run yielded dozens of functioning MECSEL devices, despite many problems in our initial implementation of this new micro-fabrication process flow.

In spite of the several shortcomings of our initial fabrication run, the MECSEL exhibited encouraging performance results. Figure 3.10 shows the slope efficiency and wall-plug efficiency (WPE) of the same 10-µm-aperture MECSEL discussed above. The slope efficiency was 0.61 W/A, which corresponds to a differential quantum efficiency (DQE) of 41%. The wall-plug efficiency reached a peak value of 8.6% at a drive current of 4.8 mA. Due to the shorter-than-intended wavelength of the dielectric DBR, all of the working MECSEL devices on this wafer operated at wavelengths shorter than 850 nm. The data shown in Figure 3.10 was measured from a MECSEL operating at 842 nm, which was a few nanometers shorter than the peak optical gain wavelength of the GaAs quantum wells. The peak gain wavelength increased rapidly as the device was heated with injection current, causing a large mismatch relative to the cavity resonance wavelength. Thus, we expected the peak output power from this device to be less than ideal.

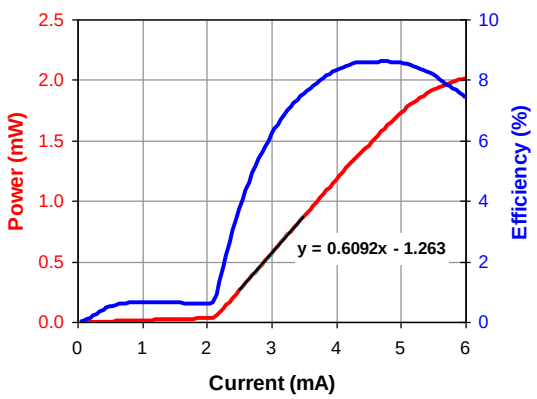

Figure 3.10. Light power and wall-plug efficiency versus current for the 10-µm-aperture MECSEL device.

In addition to the mismatch between the cavity and gain wavelengths, temperature dependent phasing in the external cavity section of the MECSEL limited the output power from the device. Because of the non-zero reflectivity of the top semiconductor DBR employed in this fabrication run, a coupled cavity existed, and the phase in the external cavity had to be a multiple of π for constructive phasing of the two top reflectors (semiconductor and dielectric DBRs). Only a fraction of the fabricated MECSELs had the proper round-trip phase in the external-cavity section to achieve low threshold current lasing at room temperature. However, due to differences in coefficients of thermal expansions (CTE) of the semiconductor and dielectric materials, and preferential heating of the semiconductor layers when current was injected into the implant aperture, the relative phasing of the two cavities depended on both ambient temperature and the injected current level. The data presented above shows a case of a MECSEL device that was properly phased at room temperature and low injection currents. As the ambient temperature was increased above 25 °C, the threshold current increased due to phase mismatching of the coupled cavities. Similarly, at high injection currents, we believe that phase mismatching also caused the output power to roll over earlier than it otherwise would have.

In the future we will attempt two alternative solutions to the coupled-cavity phasing problem. First, the coupled cavity effect can be nearly eliminated by omitting the top semiconductor DBR and anti-reflection

coating the top semiconductor facet. In that case, the external DBR reflectivity must be increased to approximately 99.5%, and the external cavity losses should be kept below 0.2%, which seems feasible. The second solution retains the coupled cavity, but adds a thin-film heater that selectively heats the external-cavity section so that the external cavity length can be increased with heat to maintain the proper phase relationship.

Finally, we discuss the single-mode performance of the MECSEL devices described above. Polarization-resolved power versus current data is shown in Figure 3.11(a), which clearly shows that the device operated in a single polarization mode up to thermal roll over. Although nothing was intentionally done to select a single polarization mode, the single polarization performance seemed relatively robust compared to that of typical VCSELs. In the future, it will be interesting to see if single-polarization operation is maintained in devices where the cavity resonance is more closely matched to the peak gain wavelength.

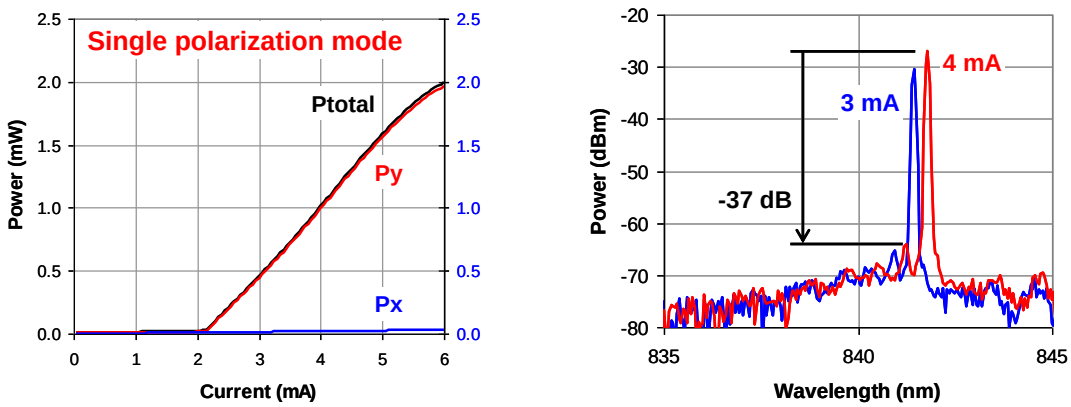

(a) (b)

Figure 3.11. (a) Polarization-resolved power versus current data, showing a threshold current of 2.1 mA and single-polarization operation to at least 6 mA. (b) Emission spectra at 3 and 4 mA drive current, showing greater than 35 dB side-mode suppression ratio.

Single transverse-mode operation was observed, as shown by the optical emission spectra in Figure 3.11(b), with side-mode suppression ratios exceeding 35 dB. Operation in a single-transverse mode was anticipated, largely based on the matched spatial overlap of the implant gain aperture and the fundamental Gaussian optical mode of the external cavity. In addition, higher order transverse modes suffered increased optical losses due to diffraction effects of the top metal aperture in the plano-concave cavity.

The short 25-µm external cavity length also yielded a large longitudinal mode spacing (14 nm) relative to the optical gain bandwidth. Thus, much like in a conventional VCSEL, single longitudinal mode operation was virtually guaranteed due to the large longitudinal mode spacing. Our measurements of emission spectra from several MECSEL devices confirmed our expectation of operation on only a single longitudinal mode.

3.5 Summary

In summary, we have demonstrated operation of a micro-external-cavity surface-emitting laser (MECSEL) emitting at wavelengths near 850 nm. We micro-fabricated the external curved mirror on top of the active semiconductor portion of the device by patterning photoresist cylinders concentric with the optical-gain apertures, and reflowing the photoresist to create photoresist domes with spherical surfaces. A dielectric DBR was deposited over the photoresist domes, and the photoresist was removed using an oxygen plasma, yielding curved dielectric mirrors suspended approximately 25 µm above the surface of

the active semiconductor layers. We measured a threshold current of 2.1 mA and differential quantum efficiency of 41% from a MECSEL with an implant aperture diameter of 10 µm. The MECSEL operated in a single polarization, transverse, and longitudinal mode up to thermal roll over at an output power of 2 mW.

The additional cavity length of the MECSEL, relative to a VCSEL, enables higher output power and narrower laser linewidth, and micro-fabrication of the external mirror preserves the manufacturing cost advantages of parallel lithographic alignment. In the near future we plan to demonstrate narrow-linewidth MECSELs suitable for use in battery-powered high-performance atomic micro-systems.

4 LINEWIDTH ENHANCEMENT FACTOR OPTIMIZATION

4.1 Introduction

We recall from Section 1.2 that the linewidth of a semiconductor laser depends on the linewidth enhancement factor α according to the formula

$$\Delta\nu = \Delta\nu_{ST}\left(1+\alpha^2\right), \tag{4.1}$$

where $\Delta\nu_{ST}$ is the modified Schawlow-Townes linewidth, due to spontaneous emission, which depends primarily on the cold-cavity linewidth and the output power of the laser as described in Section 1.2. For typical values of the linewidth enhancement factor ($\alpha \approx 3$), equation (4.1) shows that the linewidth of the laser is increased approximately 10 times above the standard quantum limit. If the linewidth enhancement factor could be reduced by a factor of 2, the linewidth would be decreased by almost 70%, so it is well worth considering how we might reduce α.

The linewidth enhancement factor α is a property of the active region material; linewidth enhancement accounts for the fact that carrier density fluctuations in the semiconductor cause refractive index fluctuations that perturb the laser frequency.[6] In this section, we apply theoretical models of the multi-quantum-well active regions to guide the design of our VCSEL gain regions.

4.2 Experimental Measurement of Alpha

In order to experimentally determine how much the linewidth of our VCSELs was broadened by the linewidth enhancement factor, we setup an apparatus to directly measure the linewidth enhancement factor (alpha) of our lasers. The linewidth enhancement factor can be experimentally determined by measuring both the amplitude modulation (AM) and frequency modulation (FM) response of a semiconductor laser to a small-signal sinusoidal modulation of the laser current.[14] The electric field of the laser can be written as

$$E(t) = E_0\left[1+\left(m/2\right)\cos\left(\Omega t\right)\right]\cos\left[\omega t + \beta\cos\left(\Omega t\right)\right], \tag{4.2}$$

where m is the AM index and β is the FM index resulting from a small-signal current modulation at frequency Ω. It can be shown that the linewidth enhancement factor α is given by the ratio

$$\alpha \approx -2\beta/m, \tag{4.3}$$

where the approximation becomes more accurate for large modulation frequencies such that $\Omega >> (n_{sp}/P_m)(1/\tau_p)$. For most semiconductor lasers of interest, modulation frequencies above about 1 GHz satisfy the requirement of equation (4.3).

Experimentally, the AM index m can be determined by using an optical power detector (photodiode) with sufficiently high bandwidth. The photodiode output is measured with an electrical spectrum analyzer (ESA), as shown schematically in Figure 4.1(a). The FM index is typically obtained by measuring the first FM sideband strength relative to the optical carrier strength using a scanning Fabry-Perot interferometer. Instead, we measured the FM sideband strength by heterodyning the VCSEL with an external-cavity diode laser (ECDL) as shown schematically in Figure 4.1(a). The ESA measurement of the photodiode output is shown in Figure 4.1(b). The amplitude of the carrier (i=0) and the first sideband (i=1) depend on the nth order Bessel functions $J_n(\beta)$ as described in reference [14]. Hence, we can determine the FM index by comparing the amplitudes of the carrier and first sideband peaks.

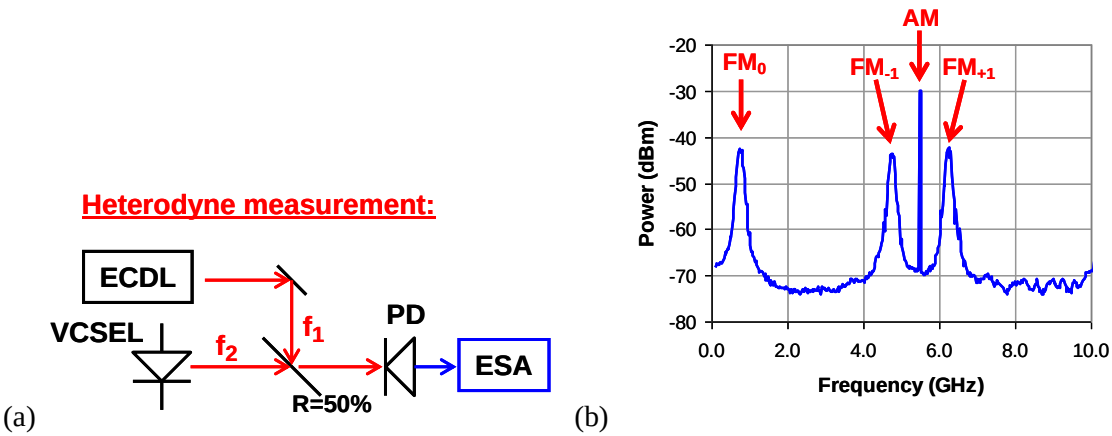

Figure 4.1. (a) Schematic of heterodyne apparatus used to measure VCSEL AM and FM modulation response. (b) Spectrum analyzer measurement of AM and FM modulation of a VCSEL.

Our standard 850-nm VCSELs contain a 5-quantum-well active region, with 8-nm-thick GaAs quantum wells separated by 8-nm thick 20% AlGaAs barrier layers. The data shown in Figure 4.1(b) was obtained with an extended-cavity VCSEL containing our standard 5-quantum-well active region. Analysis of the modulation response data yielded a linewidth enhancement factor $\alpha \approx 4$, which is typical of values reported in the literature for VCSELs with similar active regions.[15]

4.3 Quantum Well Model of the Linewidth Enhancement Factor

In this section, we discuss the quantum well modeling that was undertaken to theoretically determine the linewidth enhancement factor α, which is simply the ratio of the differential change in real dn_r to imaginary dn_i refractive index in response to a change in carrier density dN. We can write α in terms of the real refractive index and the optical gain (rather than the imaginary refractive index) as

$$\alpha = \frac{dn_r}{dn_i} = -2k\frac{d(\delta n)}{dN}\left(\frac{dG}{dN}\right)^{-1}, \qquad (4.4)$$

where k is the laser field wave-vector, δn is the carrier-induced refractive index change, N is the carrier density, and G is the optical intensity gain.[6] In the modeling, the gain and carrier-induced refractive index changes were computed using semi-classical laser theory,[16] where the quantum mechanical semiconductor gain medium was described using the semiconductor Bloch equations with collisions treated at the level of quantum kinetic equations.[17] Input to the calculation was the bandstructure, which was determined by diagonalizing the Luttinger Hamiltonian in the envelope approximation.[17]

Figure 4.2 shows two of the quantum well designs that were modeled to determine the linewidth enhancement factor dependence on the depth of the quantum wells, which here was determined by the height (composition) of the $Al_xGa_{1-x}As$ barriers since the well material was GaAs in both designs. The first quantum well design, with 20% AlGaAs barriers, was our standard VCSEL active region design. The second quantum well design, with 30% AlGaAs barriers, was motivated by a publication that empirically demonstrated smaller linewidth enhancement factors with increasing barrier heights (increasing aluminum composition AlGaAs).[18]

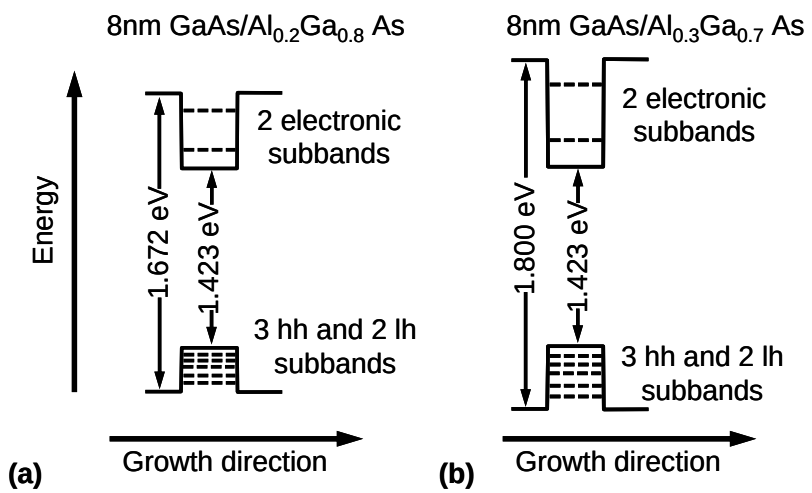

Figure 4.2. Two quantum well designs that were modeled: (a) 20% Al barriers, (b) 30% Al barriers.

Figure 4.3 shows the results of the calculations for the two quantum well designs, with (a) 20% Al barriers, and (b) 30% Al barriers. In Figure 4.3, the upper plots show the material gain versus photon energy and the lower plots show the linewidth enhancement factor (alpha) versus photon energy, for three different levels of sheet carrier density. For both designs, alpha achieves values below 1.0 for photon energies on the high side of the peak gain energy. Experimentally, we measure the laser linewidth as a

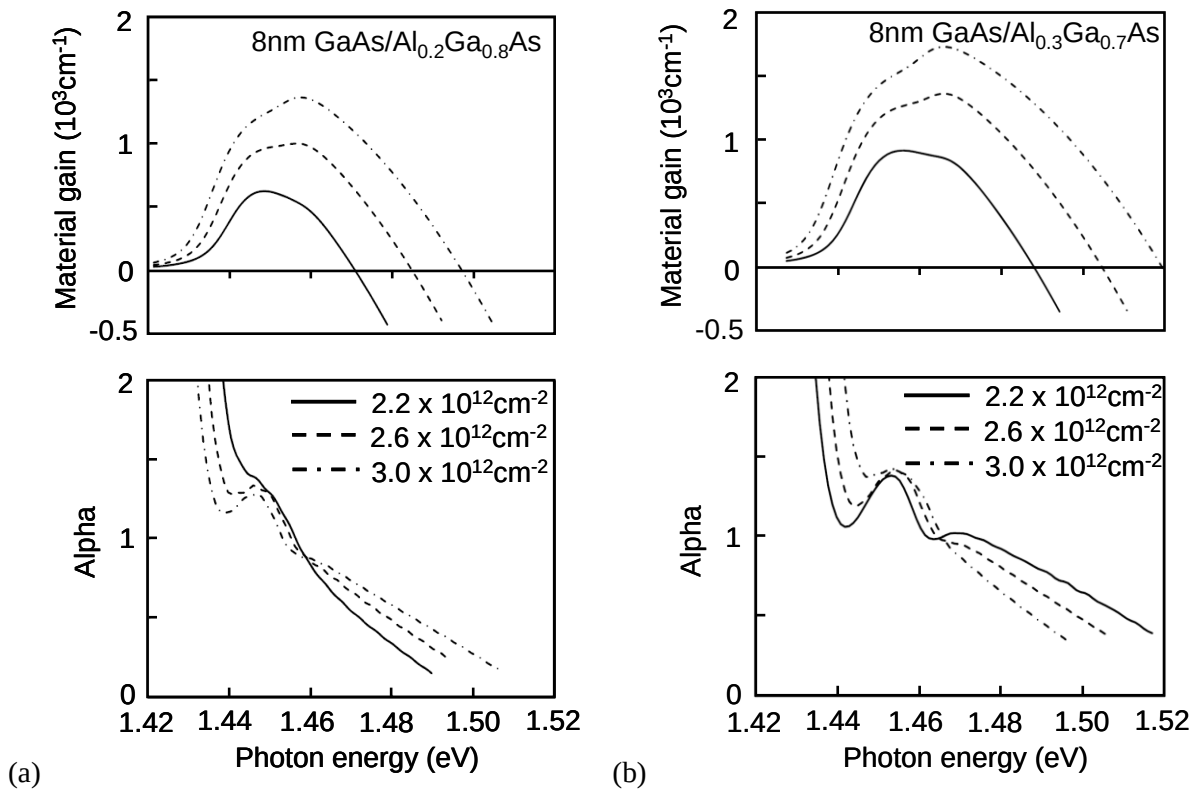

Figure 4.3. Model results for Material gain and Alpha versus Photon energy for two different quantum well designs: (a) 20% Al barriers, (b) 30% Al barriers.

function of both laser temperature and injection current, seeking a minimum value of linewidth enhancement factor. The laser temperature determines the photon energy, since it determines the cavity resonance frequency relative to the gain spectrum. We conclude based on the model results that the experimentally measured linewidth enhancement factor $\alpha \approx 4$ cannot be explained solely by the effect of the quantum wells, which would predict $\alpha \approx 1$.

The above results ignore the contribution of the barriers to the linewidth enhancement factor. In a real laser active region, which has barriers between multiple quantum wells, a more accurate description of alpha is given by

$$\begin{aligned}
\alpha &= -2\left\{ n_{qw} h \frac{d}{dN}\left(\frac{d\phi}{dz}\right)_{qw} + \left[\left(n_{qw}-1\right)h_b + 2h_c\right]\frac{d}{dN}\left(\frac{d\phi}{dz}\right)_b \right\} \\
&\quad \times \left[n_{qw} h \left(\frac{dG}{dN}\right)_{qw} + \left[\left(n_{qw}-1\right)h_b + 2h_c\right]\left(\frac{dG}{dN}\right)_b \right]^{-1} \\
&\simeq -2\left\{ n_{qw} h \frac{d}{dN}\left(\frac{d\phi}{dz}\right)_{qw} + \left[\left(n_{qw}-1\right)h_b + 2h_c\right]\frac{d}{dN}\left(\frac{d\phi}{dz}\right)_b \right\} \left[n_{qw} h \left(\frac{dG}{dN}\right)_{qw} \right]^{-1}
\end{aligned} \tag{4.5}$$

where the bottom line comes from realizing that while the barrier contribution to gain is negligible, its contribution to the refractive index can still be sizable.[19] For the barrier term in equation (4.5) we use Figure 2 from reference [20] to obtain

$$\frac{d}{dN}\left(\frac{d\phi}{dz}\right)_b = \frac{(1.2-0.3)\times 10^3 cm^{-1}}{(2-6)\times 10^{18} cm^{-3}} = -2.25\times 10^{-16} cm^2 \quad . \tag{4.6}$$

Note that within the bandgap the curves are pretty straight and evenly spaced, so we ignore the energy and carrier density dependences. For the quantum well terms, we use the computed values

$$\begin{aligned}
\frac{d}{dN}\left(\frac{d\phi}{dz}\right)_{qw} &= \frac{(0.883-1.276)\times 10^3 cm^{-1}}{(3-2)\times 10^{16} m^{-2}} \times 8\times 10^{-9} m \\
&= -\frac{0.393\times 10^3 cm^{-1}}{1.25\times 10^{18} cm^{-3}} = -3.14\times 10^{-16} cm^2 \quad \text{, and} \qquad (4.7) \\
\left(\frac{dG}{dN}\right)_{qw} &= \frac{(1.370-0.428)\times 10^3 cm^{-1}}{(3-2)\times 10^{16} m^{-2}} \times 8\times 10^{-9} m \\
&= \frac{0.942\times 10^3 cm^{-1}}{1.25\times 10^{18} cm^{-3}} = 7.536\times 10^{-16} cm^2 \quad . \qquad (4.8)
\end{aligned}$$

Figure 4.4 shows the linewidth enhancement factor determined by equation (4.5), using the values (4.6) through (4.8). The figure shows results for a 3-quantum-well gain region with varying thickness of the outer-most barrier layers. Clearly the barrier layers contribute significantly to the linewidth enhancement factor.

Based on the finding that the barrier layers contribute more than the wells to the linewidth enhancement factor, we are developing a more accurate model that will predict the linewidth enhancement factor of the multiple-quantum-well (MQW) gain region as a whole, rather than adding separate contributions from the well and barrier layers. The new model will treat both wells and barriers on the same footing, and include many-body effects in both regions. Although we don't expect to see more than a 50% change in the results, it will be reassuring to see qualitative agreement between the approximate model of the barriers described here and the fully self-consistent microscopic model under development. Based on the results of the more accurate model, we plan to grow a range of quantum well active regions, including the

optimum (minimum-alpha) active region design, and measure the linewidth enhancement factor of each design to show that the theory can in fact guide us to an optimum (minimum-alpha) VCSEL design.

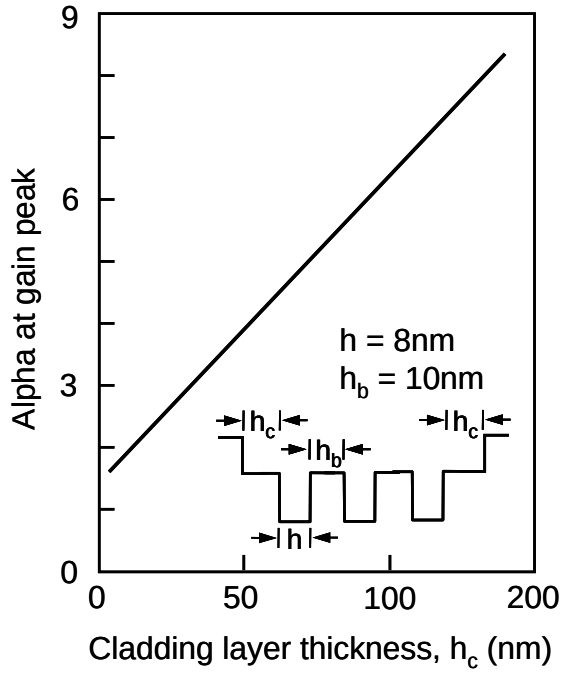

Figure 4.4. Linewidth enhancement factor at gain peak versus cladding layer thickness for carrier density between 2 to 3 x 10^{12} cm^{-2} for a structure with three 8nm GaAs QWs and 10nm $Al_{0.2}Ga_{0.8}As$ barriers. The outer barrier layers (cladding layers) are $Al_{0.3}Ga_{0.7}As$ with varying thicknesses.

4.4 Summary

Because the laser linewidth scales as the square of the linewidth enhancement factor, according to the formula $\Delta\nu = \Delta\nu_{ST}\left(1+\alpha^2\right)$, and because the linewidth enhancement factor of typical VCSEL active regions is greater than 3 (as reported in section 4.2), we conclude that the laser linewidth of typical VCSELs is a factor of 10 larger than the potentially achievable modified Schawlow-Townes linewidth $\Delta\nu_{ST}$. The theoretical models of linewidth enhancement factor, reported in section 4.3, predict that the quantum wells alone would yield a linewidth enhancement factor $\alpha \approx 1$, which would result in a 5-fold reduction in laser linewidth. The modeling further indicates that the barriers contribute more than the wells to the large linewidth enhancement factors observed in typical devices. However, we remain hopeful that in the near future the models developed under this LDRD project will guide us to new VCSEL active-region designs that yield significantly lower linewidth enhancement factors.

5 CONCLUSIONS

This report has documented our efforts to reduce VCSEL linewidths below 10 MHz to meet the needs of emerging sub-Doppler atomic microsystems, such as cold-atom traps. In the pursuit of narrower linewidths we have been mindful not to abandon the key attribute of "low power consumption" that makes VCSELs so attractive for microsystem applications. We have investigated two complementary approaches to reduce VCSEL linewidth: (A) increasing the laser-cavity quality factor, and (B) decreasing the linewidth enhancement factor (alpha) of the optical gain medium.

Under LDRD funding we developed two new VCSEL devices that achieved increased cavity quality factors: (1) all-semiconductor extended-cavity VCSELs, and (2) micro-external-cavity surface-emitting lasers (MECSELs). In section 2 we described the extended-cavity (EC) VCSEL device that achieved a five-fold reduction in VCSEL linewidth (from 50 to 8.5 MHz) primarily by adding cavity length extension layers to a standard oxide-confined 850-nm VCSEL structure. The EC-VCSEL device also yielded a single-mode output power of 2.5 mW, which is at least twice that of a typical single-mode VCSEL. Although the EC-VCSEL device offers only a limited reduction in linewidth, it has a tremendous advantage in that it only requires a few changes to the VCSEL epitaxial structure and it otherwise leverages established VCSEL micro-fabrication process techniques.[21]

In section 3 we described the new MECSEL device, which utilized wafer-scale semiconductor micro-fabrication techniques to produce thousands of external-cavity lasers on a single GaAs wafer.[22] The MECSEL fabrication process produced a microscopic curved dielectric mirror above each VCSEL device on the GaAs wafer. A typical external dielectric mirror dome had a base diameter of 160 µm, a radius of curvature of 131 µm, and rose to a height of 25 µm above the surface of the active semiconductor layers. We demonstrated a MECSEL with a 10 µm implant aperture that exhibited a threshold current of 2.1 mA, a differential quantum efficiency of 41%, and operated in a single polarization, transverse, and longitudinal mode up to thermal roll over at an output power of 2 mW. The additional cavity length of the MECSEL, relative to a VCSEL, is expected to enable higher output powers and narrower linewidths. Meanwhile, micro-fabrication of the external mirror preserves the manufacturing cost advantages of parallel lithographic alignment. In the near future we plan to demonstrate narrow-linewidth MECSELs suitable for use in battery-powered high-performance atomic micro-systems.

Finally, in section 4 we described our experimental and theoretical efforts aimed at reducing the linewidth enhancement factor of VCSEL gain regions. We learned from the theoretical models that the barrier layers contribute more to linewidth enhancement than the quantum wells themselves. We have started development of a new and more accurate model that will compute the linewidth enhancement factor of an entire gain region (quantum wells and barriers combined) including many-body effects. We plan to apply the new model to optimize the active region design of our VCSELs in order to achieve minimum linewidth enhancement.

The new VCSEL devices developed under this LDRD project have demonstrated linewidths below 10 MHz, and linewidths below 1 MHz seem feasible with further optimization. In particular, we see near-term opportunities to (1) further optimize semiconductor active regions to reduce the linewidth enhancement factor and (2) further optimize MECSEL devices to achieve higher cavity quality factors, narrower laser linewidths, and higher single-mode output powers.

6 REFERENCES

1. J. Kitching, S. Knappe, N. Vukicevic, L. Hollberg, R. Wynands, and W. Weidmann, "A Microwave Frequency Reference Based on VCSEL-Driven Dark Line Resonances in Cs Vapor," IEEE Trans. Instrum. Meas. 49, pp. 1313–1317 (2000).
2. R. Lutwak, A. Rashed, M. Varghese, G. Tepolt, J. Leblanc, M. Mescher, D. K. Serkland, and G. M. Peake, "The miniature atomic clock - Pre-production results", Proceedings of the 2007 IEEE International Frequency Control Symposium, Geneva, Switzerland, pp. 1327-1333 (2007).
3. P. D. D. Schwindt, S. Knappe, V. Shah, L. Hollberg, J. Kitching, L.-A. Liew and J. Moreland, "Chip-scale atomic magnetometer," Appl. Phys. Lett. 85, pp. 6409-6411 (2004).
4. D. K. Serkland, G. M. Peake, K. M. Geib, R. Lutwak, A. Rashed, M. Varghese, G. Tepolt, and M. Prouty, "VCSELs for atomic sensors," Proc. SPIE 6484, pp. 648406-1 to -10 (2007).
5. M.A. Holm, D. Burns, A.I. Ferguson, M.D. Dawson, "Actively Stabilized Single-Frequency Vertical-External-Cavity AlGaAs Laser," Photon. Technol. Lett., vol. 11, p. 1551 (1999).
6. C. H. Henry, "Theory of the linewidth of semiconductor lasers," IEEE J. Quantum Electronics QE-18, pp. 259-264 (1982).
7. M. A. Holm, D. Burns, A.I. Ferguson, M.D. Dawson, "Actively Stabilized Single-Frequency Vertical-External-Cavity AlGaAs Laser," IEEE Photon. Technol. Lett. 11, pp. 1551-1553 (1999).
8. A. L. Schawlow, and C. H Townes, "Infrared and Optical Masers," Physical Review 112, pp. 1940-1949 (1958).
9. J. E. Sansonetti, W. C. Martin, and S. L. Young, "Handbook of Basic Atomic Spectroscopic Data", available online at http://physics.nist.gov/PhysRefData/Handbook/, National Institute of Standards and Technology, Gaithersburg, MD (2005).
10. Daniel A. Steck, "Cesium D Line Data," available online at http://steck.us/alkalidata, revision 2.1, (2008).
11. S. Jefferts, J. Shirley, T. Parker, T. Heavner, D. Meekhof, C. Nelson, F. Levi, G. Costanzo, A. DeMarchi, R. Drullinger, L. Hollberg, W. Lee, F. Walls, "Accuracy evaluation of NIST-F1," Metrologia 39, p. 321 (2002).
12. D. K. Serkland, G. M. Peake, K. M. Geib, R. Lutwak, R. M. Garvey, M. Varghese, and M. Mescher, "VCSELs for atomic clocks," Proc. SPIE 6132, pp. 613208-1 to -11 (2006).
13. A. E. Siegman, *Lasers*, University Science Books, Sausalito, pp. 744-776 (1986).
14. C. Harder, K. Vahala, and A. Yariv, "Measurement of the linewidth enhancement factor α of semiconductor lasers," Appl. Phys. Lett. 42, pp. 328-330 (1983).
15. B. Moller, E. Zeeb, U. Fiedler, T. Hackbarth, and K. J. Ebeling, "Linewidth enhancement factor of Vertical-Cavity Surface-Emitting Laser Diodes," IEEE Photon. Technol. Lett. 11, pp. 1551-1553 (1999).
16. M. Sargent III, M. O. Scully and W. E. Lamb, Jr., *Laser Physics*, Addison-Wesley, Reading (1974).
17. W. W. Chow and S. W. Koch, *Semiconductor-Laser Fundamentals: Physics of the Gain Materials*, Springer, Berlin (1998).

18. B. Zhao, T. R. Chen, S. Wu, Y. H. Zhuang, Y. Yamada, and A. Yariv, “Direct measurement of linewidth enhancement factors in quantum well lasers of different quantum well barrier heights,” Appl. Phys. Lett. 62, pp. 1591-1593 (1993).

19. C.-Z. Ning, W. W. Chow, D. J. Bossert, R. A. Indik, and J. V. Moloney, “Influences of Unconfined States on the Optical Properties of Quantum-Well Structures,” IEEE J. Sel. Topics in Quantum Electronics 3, pp. 129-135 (1997).

20. W. W. Chow, S. W. Koch, M. Sargent III, “The Effects of Electron-Hole Coulomb Interaction in Semiconductor Lasers,” IEEE J. Quantum Electronics 26, pp. 1052-1057 (1990).

21. D. K. Serkland, G. A. Keeler, K. M. Geib, G. M. Peake, "Narrow linewidth VCSELs for high-resolution spectroscopy", Proceedings of the SPIE, vol. 7229, pp. 722907 (2009).

22. D. K. Serkland, K. M. Geib, G. A. Keeler, G. M. Peake, "Fully micro-fabricated VECSEL at 850 nm", Proceedings of the SPIE, vol. 7952, pp. 79520L (2011).

7 DISTRIBUTION

1	MS1085	Darwin K. Serkland	1742 (electronic copy)
1	MS1085	Kent M. Geib	1742 (electronic copy)
1	MS1085	Gregory M. Peake	1742 (electronic copy)
1	MS1085	Charles T. Sullivan	1742 (electronic copy)
1	MS1086	Weng W. Chow	1123 (electronic copy)
1	MS0899	Technical Library	9536 (electronic copy)
1	MS0359	D.L. Chavez, LDRD Office	1911 (electronic copy)

Sandia National Laboratories